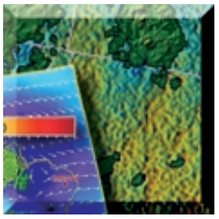

# Testing the Diagnosis of Marine Atmospheric Boundary-Layer Structure from Synthetic Aperture Radar

*Todd D. Sikora, Donald R. Thompson, and John C. Bleidorn*

A method for calculating Obukhov lengths and drag coefficients from high-resolution synthetic aperture radar (SAR)–generated wind speed imagery was tested. The wind imagery was created from six Radarsat scenes collected off the East Coast of the United States during cold air outbreaks in the winter of 1997. Comparisons were made between the drag coefficients and Obukhov lengths obtained from the SAR method and those obtained from the Tropical Ocean–Global Atmosphere Coupled Ocean–Atmosphere Response Experiment 2.5 Bulk Flux Algorithm. This algorithm uses corresponding buoy data as input. In general, the drag coefficients were in good agreement. Agreement was less precise between the two methods when comparing Obukhov lengths. It is important that the SAR imagery be inspected for the signature of convection (mottling) before implementation of the SAR method. Potential sources of disagreement between the results of the two methods are discussed. (Keywords: Air–sea interaction, Boundary-layer meteorology, Synthetic aperture radar.)

## INTRODUCTION

When the marine atmospheric boundary layer (MABL) is statically unstable, downward momentum flux occurs largely within convective downdrafts, whereas upward momentum flux occurs largely within convective updrafts.[1,2] In addition, it has been shown that within individual updraft and downdraft events, the momentum flux is asymmetric along the axis of the mean wind.[2] Larger negative momentum flux is found along the down–mean-wind edge of downdrafts and updrafts than along the up–mean-wind edge. This difference results in asymmetry in the magnitude and direction of momentum flux across updraft/downdraft couplets and therefore causes asymmetry in the patterns of centimeter-scale gravity waves on the ocean surface beneath the bases of updraft/downdraft couplets.

Synthetic aperture radar (SAR), such as the Canadian Space Agency's C-band horizontally polarized Radarsat, is sensitive to centimeter-scale sea surface roughness. SAR has the potential to be employed as a tool to help study the MABL because of its proven ability to image the sea surface footprints of convection.[3–6] References 3–5 show that a typical field of cellular convection results in a mottled appearance

on the SAR imagery. Reference 6 shows that roll convection results in linear patterns on the SAR imagery. The research presented in this article concentrated on the former type of convection.

SAR imagery can be converted to 10-m neutral wind speed imagery (hereafter referred to as wind imagery) using a scatterometer function (see the article by Thompson and Beal, this issue, and Ref. 7). A logical next step, given the research presented in Refs. 3–6, is to use wind imagery to quantitatively study MABL processes such as convection. Both our research and that of Ref. 8 employ wind imagery for just such a purpose.

Reference 8 applied a method based on Monin–Obukhov and mixed-layer similarity theory. This method uses the variance of wind imagery in the presence of statically unstable MABLs to generate diabatic wind imagery and, in the process, calculate several MABL statistics, including the Obukhov length $L$ and the drag coefficient $c_d$. It is appropriate here to briefly describe the importance of $L$ and $c_d$ to boundary-layer meteorology. The following concepts can be found in more detail in Ref. 9.

The Obukhov length can be written as

$$L = \frac{-\overline{\theta}_v u_*^3}{kgB}, \tag{1}$$

where $\overline{\theta}_v$ is the mean virtual temperature, $u_*$ is the friction velocity, $k$ is von Karman's constant (0.4), $g$ is acceleration due to gravity, and $B$ is the surface buoyancy flux. The drag coefficient $c_d$ relates the mean wind speed $V$ to $u_*$ via Eq. 2,

$$u_*^2 = c_d V^2, \tag{2}$$

and is dependent upon $L$ and the surface roughness. $L$ is a measure of the ratio of the mechanical production of turbulence to the buoyant production/destruction of turbulence. As $L$ approaches negative infinity, mechanical production dominates. As $L$ approaches zero from negative values, buoyant production dominates. As $L$ approaches zero from positive values, mechanical production of turbulence becomes increasingly damped by the statically stable stratification of the boundary layer. The static stability can therefore be related to $L$. For example, a small negative $L$ indicates a more statically unstable environment than is indicated by a larger negative $L$.

The static stability of the surface-layer and mixed-layer portions of the MABL can be related to each layer's turbulence statistics via Monin–Obukhov and mixed-layer similarity theory. Turbulence-scale horizontal variability of wind speed is related to surface-layer static stability through a combination of these two theories. Thus, application of these standard similarity theories to SAR-derived wind speed statistics should yield quantitative information about the structure of the MABL.

Note that many geophysical processes other than convection can also cause variance in SAR imagery and, hence, in wind imagery. For example, surface waves,[10] internal waves,[11] oceanographic frontal boundaries,[12] atmospheric gravity waves,[13] and mesoscale wind streaks (an example of which is shown in the next section) have all been observed in SAR imagery of the sea surface. These processes can contaminate wind speed estimates and subsequent estimates of MABL statistics. It is important, therefore, to wisely choose the SAR imagery with which to calculate MABL statistics. Simple inspection of the SAR imagery for the homogeneous presence of the mottled signature of convection, along with a choice of pixel size that minimizes unwanted small-scale variance, are steps toward this requirement. These topics are discussed in the next section.

The data set of Ref. 8 was limited to environments with low wind speeds and small air–sea temperature differences. The present research extends that work to larger wind speeds and air–sea temperature differences. No *in situ* turbulence data were concurrent with the SAR data set used in our research. However, several National Oceanic and Atmospheric Administration (NOAA) National Data Buoy Center (NDBC) buoys were present in the imaged areas. SAR-derived MABL statistics were therefore compared with statistics produced by the Tropical Ocean–Global Atmosphere Coupled Ocean–Atmosphere Response Experiment (COARE) 2.5 Bulk Flux Algorithm, which uses the buoy data as input.[14] Thus the research presented in this article should be viewed as a test of a method that, if successful, can compete with COARE 2.5 buoy estimates of MABL statistics.

## PROCEDURES

### The SAR Method

The key variable used as input for the SAR method is the ratio of variance to mean stress of the wind imagery resulting from MABL convection. This variance $\sigma_u^2$, combined with the SAR-derived estimate of MABL depth $z_i$ (based on the technique presented in Ref. 4) and the SAR-derived $u_*$ (from the wind imagery), is used to calculate $L$, which can be written as

$$L = -z_i / \{[(\sigma_u / u_*)^2 - 4] / 0.6\}^{3/2}. \tag{3}$$

$L$ is used, in turn, to calculate a diabatic $c_d$:

$$c_d = \{k / [\ln(z / z_0) - \Psi_m(z / L)]\}^2. \tag{4}$$

In Eq. 4, $z$ is the instrument height, $z_0$ is surface roughness length calculated following Ref. 15, and $\Psi_m$ is the stratification function given by Ref. 16. The family of equations is solved by iteration, with refined values of $L$ resulting in refined values of $c_d$ and, using Eq. 1, refined values of wind speed.

## Data

In this research we used six narrow ScanSAR scenes extracted from three Radarsat overpasses off the East Coast of the United States. Figure 1 shows these six scenes. The top of each scene is directed toward 348°. The scenes from the three overpasses were collected on 14 and 17 January and 6 March 1997, all at about 2254 UT. These overpasses were chosen because they were concurrent with strong cold air outbreaks. The red star in each scene represents the position of NDBC buoys at the time of the overpasses. Buoy latitude and longitude are given in the figure caption. The corresponding buoy measurements of $V$, average air temperature $T_a$, and average sea surface temperature $T_s$ are also provided with each scene. All buoy averaging times for the data presented here are 8 min and are calculated just prior to the top of an hour. Therefore, the times of the buoy averages correspond almost identically to the times of the SAR overpasses.

The six scenes of interest in the present research are subimages of the full overpasses shown in Fig. 2. Each of these overpasses was produced at the Canadian Space Agency's Gatineau facility. Calibration (conversion from raw data to normalized radar cross section, NRCS) of the ScanSAR imagery is generally very difficult; in particular, calibration coefficients for the six overpasses of interest here are not accurate (see Vachon et al. and Katsaros et al., this issue). In an attempt to overcome this difficulty, we converted the six overpasses to wind imagery using the Gatineau calibration coefficients, the wind direction from the relevant buoy from each subscene, and the procedure discussed by Thompson and Beal (this issue). We then scaled the resulting wind imagery to the mean wind speed as measured by the buoy.

The conversion from NRCS to wind imagery must be done cautiously. One reason for caution is that the relationship between NRCS and wind speed is highly dependent on the near-surface wind direction (Thompson and Beal, this issue; Ref. 7). The near-surface wind direction over the ocean can be quite variable, especially at high resolution in convective environments. Moreover, enhanced or decreased backscatter due to oceanographic noise, speckle noise, or both can contaminate the SAR wind estimate.[8] Thus, when converting SAR imagery to wind imagery, application of some spatial smoothing is usually desirable. This smoothing minimizes contaminating variance while still providing a resolution high enough to preserve

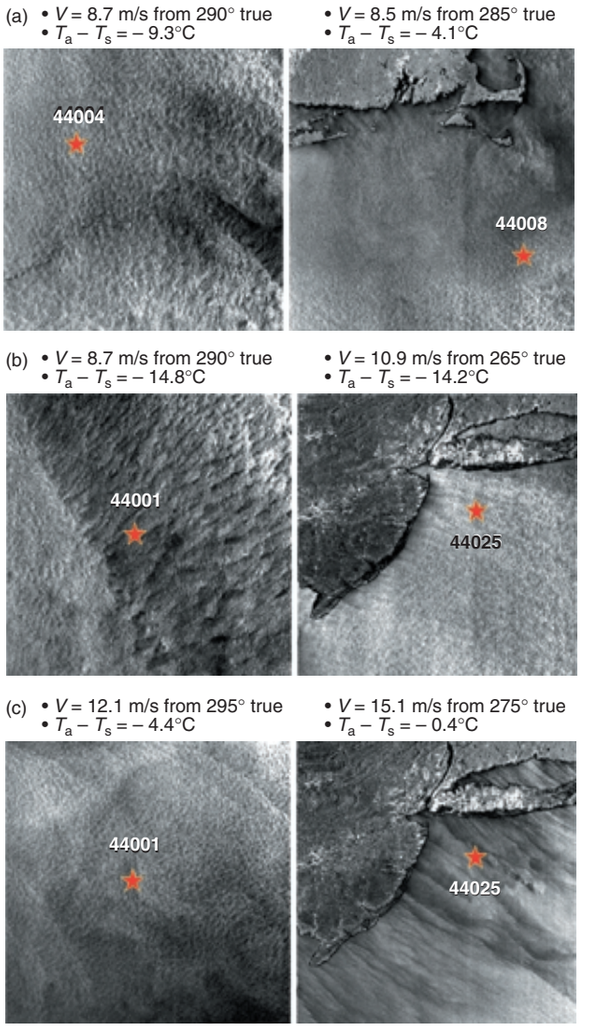


**Figure 1.** SAR scenes and embedded buoy locations (denoted by red stars) for (a) 14 January 1997, (b) 17 January 1997, and (c) 6 March 1997. Top of each scene is directed toward 348°. Corresponding buoy average wind speeds $V$ and differences between air temperature $T_a$ and average sea surface temperature $T_s$ are shown on each scene. All buoy averaging times are 8 min, calculated just prior to the top of an hour, so that times of buoy averages nearly correspond to SAR overpasses. Buoy locations are as follows: 44004, 38.46°N, 70.69°W; 44008, 40.50°N, 69.43°W; 44001, 34.68°N, 72.64°W; and 44025, 40.25°N, 73.17°W.

MABL convective signatures. For our research we adopted a 300-m pixel size; however, additional work is needed to test the validity of the choice.

Using the 8-min average buoy wind speeds and invoking Taylor's hypothesis, portions of each resulting wind image were cropped so that the spatial data from the resulting subscene could be compared with the temporal data of the buoy. These square subscenes ranged in area from 17.6 to 51.8 km$^2$ and were used as input for the SAR method.

Because $L$ and $c_d$ are key parameters in the SAR method, we present comparisons of $L$ and 5-m $c_d$ values

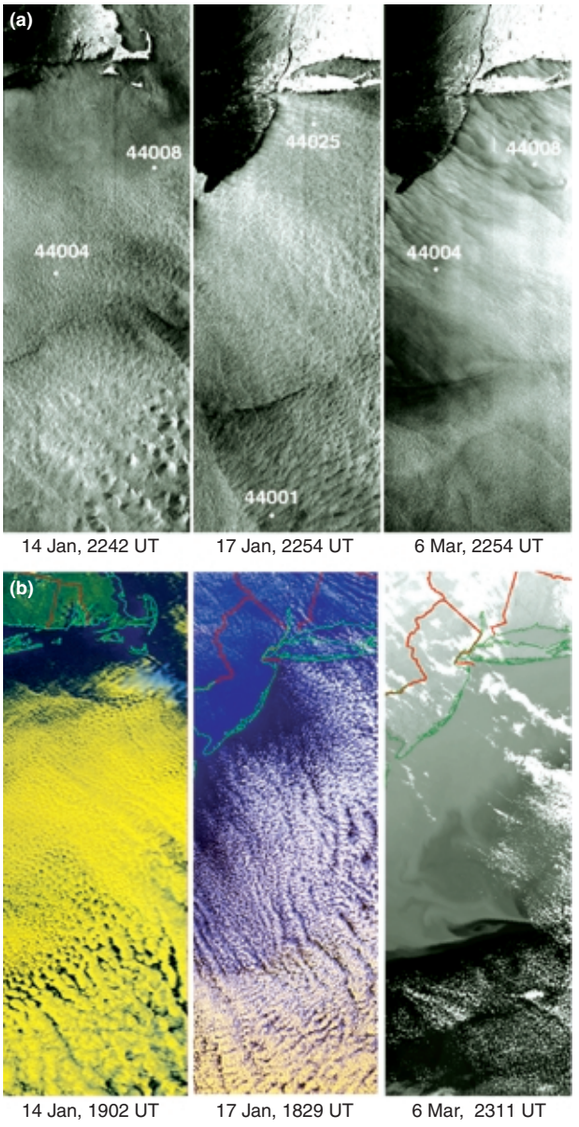


**Figure 2.** (a) SAR overpasses with (b) corresponding Advanced Very High Resolution Radiometer (AVHRR) imagery. Buoy locations are the same as those given in Fig. 1. Radarsat and AVHRR swath widths are all 300 km.

from the SAR method with corresponding $L$ and 5-m $c_d$ values from the COARE 2.5 method ($L$ is constant in the atmospheric surface layer, where the surface layer is loosely defined to be the bottom 10% of the MABL). For the purposes of calculating $L$ and $c_d$ from the COARE 2.5 method, buoy measurements used are $V$ at 5 m, $T_a$ at 4 m, $T_s$, and average sea-level pressure. Relative humidity is also a necessary input for calculating $L$ and $c_d$, because the surface-layer humidity gradient can have a large effect on the surface-layer static stability, especially when wind speeds are low. Because the buoys used here do not measure relative humidity, a value of 100% was used for all cases. As expected, given the high wind speeds in this study, the output of the COARE 2.5 method showed little sensitivity to the relative humidity value used.

The COARE 2.5 method also requires an estimate of $z_i$ values as input. These values were found using the technique presented in Ref. 4. The COARE 2.5 method's estimates of $L$ and $c_d$ were found to be rather insensitive to the value of $z_i$ used as input. Varying $z_i$ from 500 to 2000 m in these cases caused $L$ and $c_d$ to vary by 5% at most. As is discussed in the following, and as is evident from inspection of Eq. 3, the SAR method's output of $L$ was linearly proportional to the estimate of $z_i$.

## RESULTS

Results of the SAR method and the COARE 2.5 method are given in Table 1, along with corresponding average air–sea temperature differences and wind speeds. The $L$ values generated by the SAR method exceeded those generated by the COARE 2.5 method for cases 1, 3, and 4. These three cases corresponded to the most unstable $L$ values generated by COARE 2.5. The opposite was true for cases 2, 5, and 6. Differences between the $L$ values of the two methods ranged from 19% for case 3 to a difference of 2 orders of magnitude for case 6. The $c_d$ values generated by the two methods were in better agreement than the $L$ values. Differences ranged from 3% for cases 3, 4, and 5 to 14% for case 6.

## DISCUSSION

### Drag Coefficients

The differences between the $c_d$ calculations of the two methods can be explained by analyzing Eq. 4. A similar form of Eq. 4 is used to calculate the drag coefficient from the COARE 2.5 method. Governing Eq. 4 are the roughness length term and the stratification function. Assuming that the wind imagery and the stress fields were created properly, differences between the $c_d$ results of the two methods arise mainly from differences in each method's estimate of the $L$ and, hence, the stratification function. However, as the wind speed increases, the importance of the stratification function decreases in comparison with the roughness length term. Therefore, at lower wind speeds, differences in $L$ manifest themselves as differences in $c_d$ more than at higher wind speeds.

Examining the results, one sees that wind speeds were lowest for cases 1, 2, and 3. Differences in $c_d$ were larger for cases 1 and 2 than for case 3, which had a wind speed identical to that of case 1. However, the $L$ values of case 3 were in much better agreement than those of case 1. Case 6 was the highest wind speed case, and the $c_d$ results of the two methods differed the most. The reason is the 2-order-of-magnitude difference between the $L$ values for the two methods.

**Table 1. Comparison of Obukhov lengths *L* and the drag coefficients $c_d$ at 5 m generated by the COARE 2.5 and SAR methods.**

| Case | Buoy and date | Avg. difference between air and sea surface temperature at buoy, $T_a - T_s$ (°C) | Buoy mean wind speed, *V* (m/s) | Obukhov length, *L* (m) | | Drag coefficient, $c_d$ | |
|---|---|---|---|---|---|---|---|
| | | | | COARE | SAR | COARE | SAR |
| 1 | 44004 14 Jan 97 | –9.3 | 8.7 | –26.7 | –36.7 | 0.0017 | 0.0016 |
| 2 | 44008 14 Jan 97 | –4.1 | 8.5 | –52.2 | –33.5 | 0.0015 | 0.0016 |
| 3 | 44001 17 Jan 97 | –14.8 | 8.7 | –16.5 | –20.3 | 0.0017 | 0.0017 |
| 4 | 44025 17 Jan 97 | –14.2 | 11.0 | –33.9 | –52.7 | 0.0018 | 0.0018 |
| 5 | 41001 6 Mar 97 | –4.4 | 12.1 | –123.6 | –76.8 | 0.0018 | 0.0018 |
| 6 | 44025 6 Mar 97 | –0.4 | 15.1 | –2197.0 | –38.9 | 0.0019 | 0.0022 |

## Obukhov Lengths

Case 6 stands out in this group of comparisons of *L* as one where the SAR method apparently was least effective. Given the small air–sea temperature difference and the high wind speed reported by the buoy, and given that there was no visual evidence of convection on the SAR image near the buoy, the COARE 2.5 method correctly deduced that the MABL stability was neutral at the time of the SAR overpass. Visual inspection of the wind imagery for this case indicated a large amount of streakiness in the direction of the wind reported by the buoy. The variance due to this streakiness is, of course, included as convective variance in Eq. 3. Hence, the SAR method overestimated the convective variance and calculated an *L* much larger than that calculated by the COARE 2.5 method. As stated earlier, caution is therefore required when employing the SAR method. Before invoking this technique, one must check to make certain that the mottled signature of convection is present in the imagery.

The images corresponding to cases 1 through 5 did contain signatures of MABL convection. Both the SAR method and the COARE 2.5 method indicated that case 3 was the most unstable and case 5 was the least unstable. However, the trend from most unstable to least unstable was not consistent between the two methods. The differences between the two trends occurred at cases 1, 2, and 4. Recall that for cases 1, 3, and 4, the SAR method's *L* calculations exceeded those of the COARE 2.5 method.

These observations are preliminary. Given the small sample size, it is difficult to assign causes for the observed differences in results of the two methods. However, several candidates for causes of the observed differences do exist and are outlined here.

The difference between the results of the two methods may lie with Eq. 3. Note that *L* as calculated by the SAR method is a function of the variance of the near-surface wind. The corresponding statistic used by the COARE 2.5 method is the air–sea temperature difference. It follows that if MABL convection is being forced by nonsurface processes, such as cloud radiative cooling or precipitation evaporation, the COARE 2.5 method may not accurately determine *L*.

NOAA's Advanced Very High Resolution Radiometer (AVHRR) imagery was acquired over the region of the six SAR scenes. Figure 2 shows these AVHRR images, along with corresponding SAR overpasses. Inspection of the AVHRR imagery indicates that stratocumulus clouds and/or mesoscale cellular convection were present during all cases except case 6. The presence of convective clouds leaves open the possibility that cloud radiative cooling and/or evaporative cooling were adding to the instability of the MABL. This may explain some of the differences seen in the results of the two methods.

A potentially large source of error for the SAR method is the estimate of $z_i$ from the SAR imagery using the technique presented in Ref. 4. This technique has been verified only on a limited data set in which the MABL was moderately convective. No independent measures of $z_i$ were available for our research. It is evident from Eq. 3 that errors in the estimate of $z_i$ will lead to similar errors in *L*.

As noted earlier, another potential source of error for the SAR method is the presence of extraneous variance due to oceanographic contamination of the SAR image. For the SAR method, the presence of oceanographic phenomena can produce erroneous results during the conversion from NRCS to wind imagery.

This is because the oceanographic phenomena can modulate the centimeter-scale gravity waves, thereby producing a different NRCS for a given wind speed and wind direction than would be present in their absence. Because the scale of the oceanographic contamination is expected to be less than a few hundred meters or so, we accounted for its presence by smoothing to 300-m pixels. Work to refine this procedure is ongoing.

The presence of either a young sea or swell will cause differential stress across the ocean surface for a given wind speed and direction. This differential stress is a source of contamination that can result in a breakdown of the Monin–Obukhov similarity methods for determining MABL statistics.[17] Analysis of surface wave spectra and meteorological data from the NDBC buoys indicated that cases 2 and 3 corresponded to old seas, while cases 4, 5, and 6 corresponded to young seas. Swell was present during cases 3 and 5. Surface wave spectra were not available for case 1. Because the SAR and COARE 2.5 methods both rely on Monin–Obukhov similarity theory, any error due to the presence of a young sea or swell would be found in both sets of output and therefore cannot be quantified here.

## SUMMARY

Previous research presented a method based on Monin–Obukhov and mixed-layer similarity theory that employs SAR-derived 10-m neutral wind imagery in the presence of statically unstable MABLs to calculate several MABL statistics.[8] The research presented here tested this method on six subscenes from three Radarsat overpasses off the East Coast of the United States in the presence of cold air outbreaks. Results from the SAR method ($L$ and $c_d$) were compared with those calculated using the COARE 2.5 Bulk Flux Algorithm. Data from NDBC buoys located in the SAR scenes of interest provided input for the COARE 2.5 method.

It is clear that if the mottled SAR signature of convection is absent, the SAR method can give erroneous results for $L$. This occurred in our case 6. For the remaining five cases, both the SAR method and the COARE 2.5 algorithm agreed on which cases were most and least unstable. However, case-to-case trends from most to least unstable differed in the results from the two methods. The values for $c_d$ generated by the two methods were in much better agreement than those for $L$. The largest difference between the two methods (14%) occurred when the mottled signature of convection was absent from the wind imagery (case 6).

Possible reasons for the observed differences in the output of the two methods include the presence of nonsurface forced convection, the estimate of $z_i$ from the spectrum of the wind image, the presence of oceanographic contamination biasing the wind-variance estimate, and the breakdown of Monin–Obukhov similarity theory in the presence of young seas and swell.

Future work will continue to test the SAR method on mottled wind imagery. It is evident that optimal evaluation of the SAR method described here will require a spatially robust turbulence data set from which eddy correlation statistics can be calculated.

## REFERENCES


[1] Khalsa, S. J. S., and Greenhut, G. K., "Conditional Sampling of Updrafts and Downdrafts in the Marine Atmospheric Boundary Layer," *J. Atmos. Sci.* **42**, 2250–2562 (1985).

[2] Sikora, T. D., and Young, G. S., "Observations of Planview Flux Patterns Within the Convective Marine Atmospheric Boundary Layer," *Boundary-Layer Meteorol.* **65**, 273–288 (1993).

[3] Sikora, T. D., Young, G. S., Beal, R. C., and Edson, J. B., "On the Use of Spaceborne Synthetic Aperture Radar Imagery of the Sea Surface in Detecting the Presence and Structure of the Convective Marine Atmospheric Boundary Layer," *Mon. Weather Rev.* **123**, 3623–3632 (1995).

[4] Sikora, T. D., Young, G. S., Shirer, H. N., and Chapman, R. D., "Estimating Convective Boundary Layer Depth from Microwave Radar Imagery of the Sea Surface," *J. Appl. Meteor.* **36**, 833–845 (1997).

[5] Zecchetto, S., Trivero, P., Fiscella, B., and Pavese, P., "Wind Stress Structure in the Unstable Marine Surface Layer Detected by SAR," *Boundary-Layer Meteorol.* **86**, 1–28 (1998).

[6] Mourad, P. D., "Inferring Multiscale Structure in Atmospheric Turbulence Using Satellite-Based Synthetic Aperture Radar Imagery," *J. Geophys. Res.* **101**, 18,433–18,449 (1996).

[7] Lehner, S., Horstmann, J., Koch, W., and Rosenthal, W., "Mesoscale Wind Measurements Using Recalibrated ERS SAR Images," *J. Geophys. Res.* **103**, 7847–7856 (1998).

[8] Young, G. S., Sikora, T. D., and N. S. Winstead, "On Inferring Marine Atmospheric Boundary Layer Properties from Spectral Characteristics of Satellite-borne SAR Imagery," *Mon. Weather Rev.* (in press).

[9] Panofsky, H. A., and Dutton, J. A., *Atmospheric Turbulence*, Wiley-Interscience, New York (1984).

[10] Monaldo, F. M., "On the Use of Speckle Statistics for the Extraction of Ocean Wave Spectra from SAR Imagery," in *Proc. 1988 Int. Geosci. Remote Sens. Symp.*, IEEE 88CH-2497-6, pp. 133–135, Edinburgh, Scotland (1988).

[11] Porter, D. L., and Thompson, D. R., "Continental Shelf Parameters Inferred from SAR Internal Wave Observations," *J. Atmos. Oceanic Tech.* **16**, 475–487 (1999).

[12] Nilsson, C. S., and Tildesley, P. C., "Imaging of Oceanic Features by ERS 1 Synthetic Aperture Radar," *J. Geophys. Res.* **100**, 953–967 (1995).

[13] Thomson, R. E., Vachon, P. W., and Borstad, G. A., "Airborne Synthetic Aperture Radar Imagery of Atmospheric Gravity Waves," *J. Geophys. Res.* **97**, 14,249–14,257 (1992).

[14] Fairall, C. W., Bradley, E. F., Rogers, D. P., Edson, J. B., and Young, G. S., "Bulk Parameterization of the Air–Sea Fluxes for Tropical Ocean–Global Atmosphere Response Experiment," *J. Geophys. Res.* **101**, 3747–3764 (1996).

[15] Smith, S. D., "Coefficients for Sea Surface Wind Stress, Heat Flux, and Wind Profiles as a Function of Wind Speed and Temperature," *J. Geophys. Res.* **93**, 15,467–15,472 (1988).

[16] Paulson, C. A., "The Mathematical Representation of Wind Speed and Temperature Profiles in the Unstable Atmospheric Surface Layer," *J. Appl. Meteor.* **9**, 857–861 (1970).

[17] Donelan, M. A., Drennan, W. M., and Katsaros, K. B., "The Air–Sea Momentum Flux in Conditions of Wind Sea and Swell," *J. Phys. Oceanogr.* **27**, 2087–2099 (1997).


ACKNOWLEDGMENTS: The authors are grateful to Dr. George S. Young for useful discussions covering this research. Support for this work comes from Office of Naval Research grants N00014-96-1-0376, N00014-98-WR30167, and N00014-99-WR30043.

## THE AUTHORS


TODD D. SIKORA is with the United States Naval Academy, Annapolis, MD. His e-mail address is sikora@nadn.navy.mil.

DONALD R. THOMPSON is with The Johns Hopkins University Applied Physics Laboratory, Laurel, MD. His e-mail address is donald.thompson@jhuapl.edu.

JOHN C. BLEIDORN recently completed studies at the United States Naval Academy, Annapolis, MD. He is currently serving onboard ship with the Navy.